Biomedical Instrumentation

Prof. Dr. Nizamettin AYDIN

naydin@yildiz.edu.tr

naydin@ieee.org

http://www.yildiz.edu.tr/~naydin

1

Medical Imaging Systems

Figure 12.1 Scanning lines and round objects (a) Each object represents 1 pixel, but each cycle of output signal represents 2 pixels, (b) For 2*n* scanning lines, *n* vertical objects are required, (c) If objects are located between scanning lines, 2*n* lines are insufficient, (d) For adequate resolution, 2*n*(1.4) lines are required.

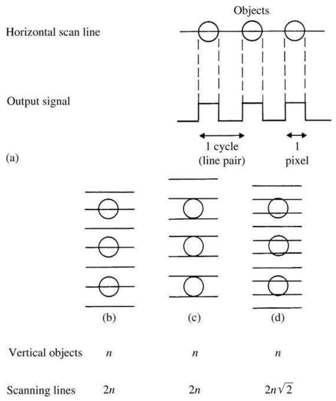

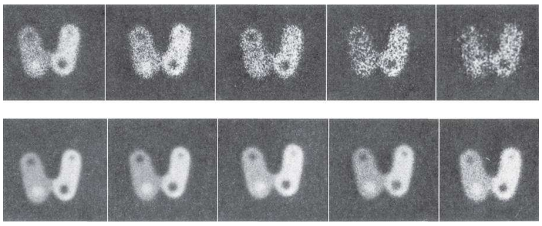

$$N = A\left(\frac{7.2}{d(C-0.05)}\right)^2$$

Figure 12.2 In each successive gamma-camera picture of a thyroid phantom, the number of counts is increased by a factor of 2. The number of counts ranges from 1536 to 800,000. The Polaroid camera aperture was reduced to avoid overexposure as the number of counts was increased.

For the Poisson probability density distribution, calculate *p*(*K*;*m*) for *K* = 0, 1, 2, 3, 4, 5 and *m* = 3.

$$p(K;m) = \frac{e^{-m} m^k}{K!}$$

K	m	P(k; m)
0	3	0.049787
1	3	0.149361
2	3	0.224042
3	3	0.224042
4	3	0.168031
5	3	0.100819

Figure 12.3 Modulation transfer function *S*(*f*) for a typical x-ray system *S*(*f*) is squared and integrated to yield *Ne*, the noise-equivalent bandwidth. The limiting resolution, 4 cycles/mm, is indicated at the 0.05 contrast level. The abscissa is plotted in cycles per millimeter, which is the same as line pairs per millimeter.

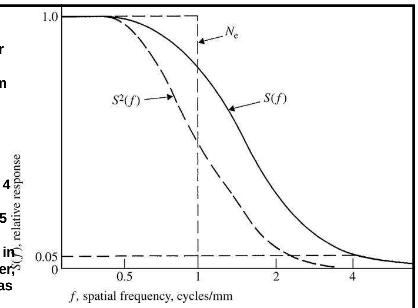

$$S(f) = \frac{\pi}{4}\left[M(f) + \frac{M(3f)}{3} - \frac{M(5f)}{5} + \frac{M(7f)}{7} - \cdots\right]$$

$$N_e = \int_0^{\infty} S^2(f)\,df$$

$$\frac{1}{N_e} = \left[\left(\frac{1}{N_{e1}}\right)^2 + \left(\frac{1}{N_{e2}}\right)^2 + \cdots\right]^{1/2}$$

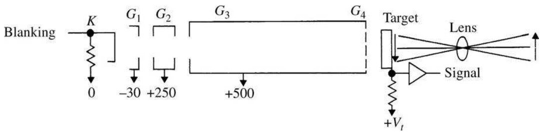

Figure 12.4 The vidicon has a cathode and a series of grids to form, shape, and control an electron beam. Magnetic deflection (not shown) scans the beam over the target, which is mounted on the interior of the glass face plate. From the target, light-modulated signal current flows through the load resistor and is amplified.

$$J_1 = AT^2 e^{-u/kT}$$

$$J_2 = BV^{3/2}$$

$$\sigma T^4 = I^2 R$$

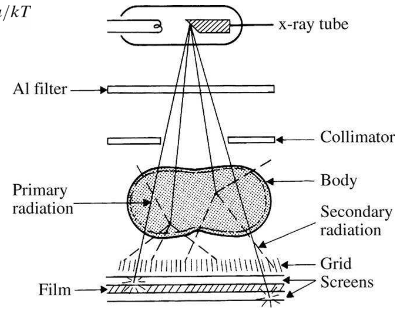

Figure 12.5 The x-ray tube generates x rays that are restricted by the aperture in the collimator. The Al filter removes low-energy x rays that would not penetrate the body. Scattered secondary radiation is trapped by the grid, whereas primary radiation strikes the screen phosphor. The resulting light exposes the film.

Figure 12.6 The lowest-energy x rays are absorbed in the anode metal and the tube glass envelope. An Al filter further reduces the low-energy x rays that do not pass through the body and would just increase the patient dose. Only the highest-energy x rays are capable of penetrating the body and contributing to the film darkening required for a picture. Note that the average energy increases with the amount of filtration.

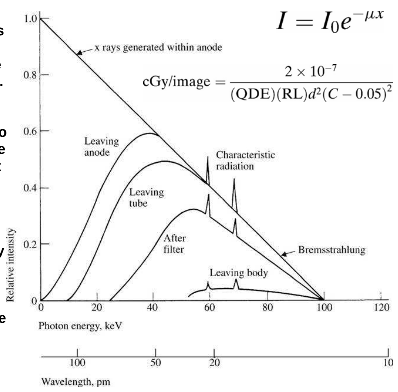

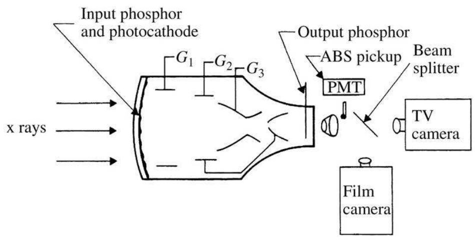

Figure 12.7 In the image intensifier, x rays strike the input phosphor screen, thus generating light. Light stimulates the photocathode to emit electrons, which are accelerated through 25 kV to strike the output phosphor screen. Brightness gain is due to both geometric gain and electronic gain.

Figure 12.8 Table-top Computed Radiography Cassette Scanner. The screen is removed from the cassette, scanned, erased and returned to the cassette for the next exposure. The image information is sent to a computer for display and analysis. Photo courtesy of iCRco.

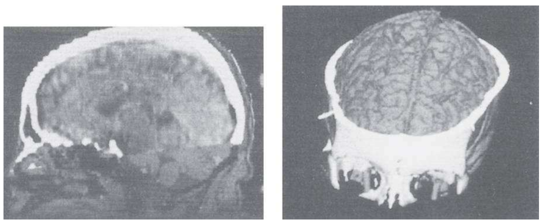

Figure 12.9 Images of the skull taken using CT and images of the brain taken with MRI, fused into composite images. (Courtesy of Rock Mackie, University of Wisconsin.)

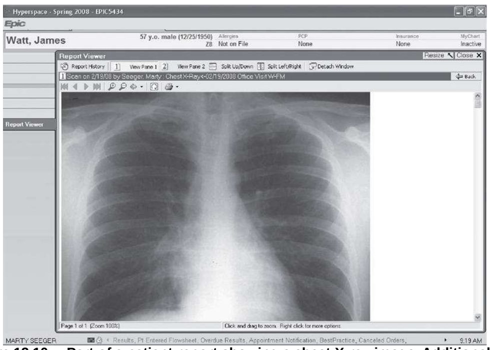

Figure 12.10 Part of a patient report showing a chest X-ray image. Additional pages would give further diagnostic image and reference other images and reports. Copyright © 2008 Epic Systems Corporation.

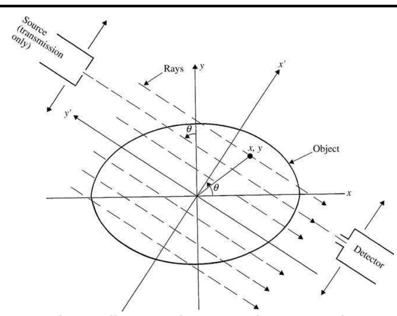

Figure 12.11 Basic coordinates and geometry for computed tomography The projection rays shown represent those measured at some angle θ. The source and detector pair are rotated together through a small angle, and a new set of rays measured. The process is repeated through a total angle of 180°. (From R. A. Brooks and G. Di Chiro, "Theory o f image reconstruction in computed tomography." *Radiology,* 1975, 117, 561-572.)

$$I^{\theta k} = I_0 \exp\left(-\sum_{ij} W_{ij}^{\theta k}\mu_{ij}\right)$$

$$P^{\theta k} = \ln\left(\frac{I_0}{I^{\theta k}}\right) = \sum_{ij} W_{ij}^{\theta k}\mu_{ij}$$

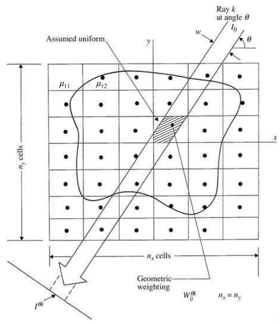

Figure 12.12 The basic parameters of computerized image reconstruction from projections. Shown are the picture element cells *mij*, a typical projection ray *Iqk*, and their geometrical overlap . (From Ernest *L.* Hall, *Computer Picture Processing and Recognition.* New York: Academic, 1978.)

Figure 12.13 Back projection (a) Projections of this object in the two directions normal to the *x* and *y* axes are measured, (b) These projection data are projected back into the image plane. The area of intersection receives their summed intensities. It is apparent that the back-projected distribution is already a crude representation of the imaged object. (From R. A. Brooks and *G.* Di Chiro, "Theory of image reconstruction in computed tomography," *Radiology,* 117, 1975, 561–572.)

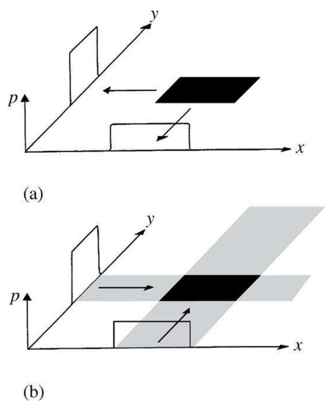

The sums of the projection data for *x* and *y* are equal, as shown in Fig. 12.13(a). The sum of the projection data (1.0 or 0) is divided evenly over each block (1/3 or 0) for *x* and *y* and the results added to yield the backprojection shown.

0	1/3	0
1/3	2/3	1/3
0	1/3	0

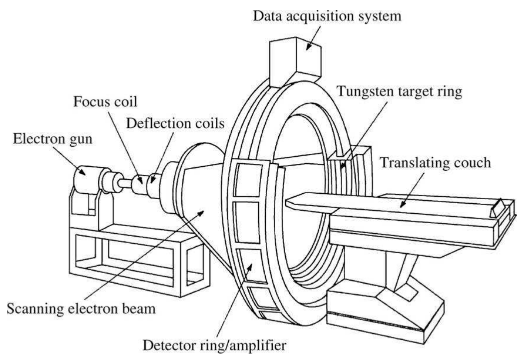

Figure 12.14 IMATRON electron beam CT system. (Courtesy of Doug Boyd, IMATRON Corp.)

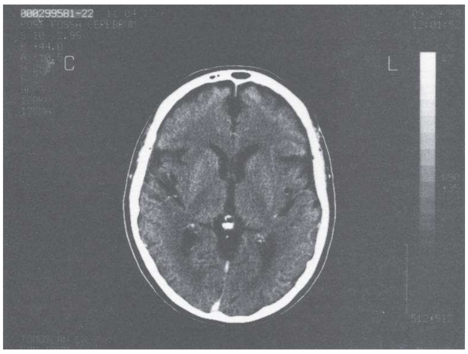

Figure 12.15 512 ´ 512 pixel CT Image of the brain Note that the increased number of pixels yields improved images. (Photo Courtesy of Philips Medical Systems.)

Figure 12.16 Control console and gantry assembly of a CT system (Photo courtesy of Philips Medical Systems.)

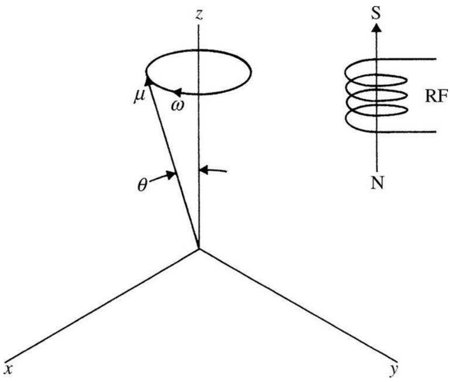

Figure 12.17 Precession of charged particles in a magnetic field

Table 12.1 Nuclear Magnetic Resonance Frequencies of Common Biological Elements

Element	Percent of Body Weight	Isotope	Relative Sensitivity	NMR Frequency, MHz/T
Hydrogen	10	^{1}H	1.0	42.57
Carbon	18	^{13}C	1.6×10^{-2}	10.70
Nitrogen	3.4	^{14}N	1.0×10^{-3}	3.08
Sodium	0.18	^{23}Na	9.3×10^{-2}	11.26
Phosphorous	1.2	^{31}P	6.6×10^{-2}	17.24

Table 12.1

Figure 12.18 MRI image of the head. Sets of images may be acquired for 1 mm section thickness at 2 mm apart for diagnosis of the entire volume of the brain. Photo courtesy of Siemens Medical.

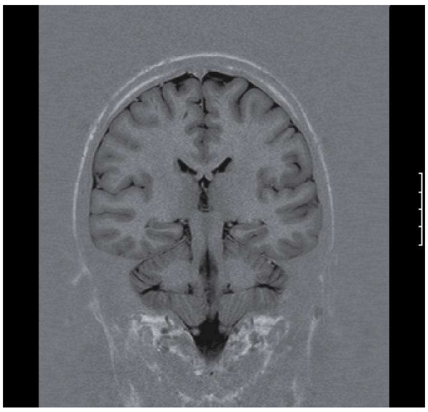

Figure 12.19 MRI image of the brain. Compare to Figure 12.15. The MRI image shows differences due to hydrogen concentration rather than tissue density making the bony part of the skull transparent and having a different contrast pattern than the CT image. Image courtesy of Siemens Medical Systems.

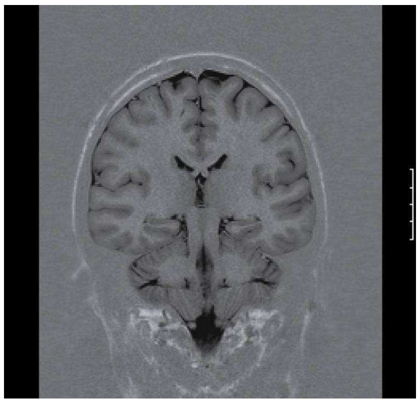

Figure 12.20 Basic implementation of a NaI scintillation detector, showing the scintillator, light-sensitive photomultiplier tube, and support electronics. (From H. N. Wagner, Jr., ed., *Principles of Nuclear Medicine.* Philadelphia: Saunders, 1968. Used with permission of W. B. Saunders Co.)

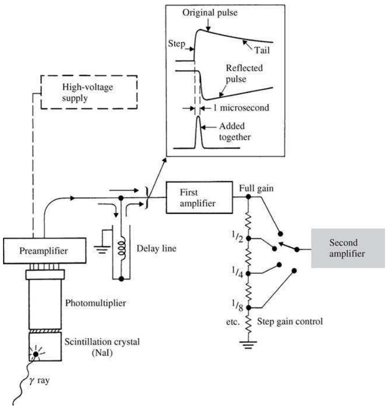

Figure 12.21 Cross section of a focusing collimator used in nuclear-medicine rectilinear scanning. The contour lines below correspond to contours of similar sensitivity to a point source of radiation, expressed as a percentage of the radiation at the focal point. (From G. J. Hine, ed., *Instrumentation in Nuclear Medicine.* New York: Academic, 1967.)

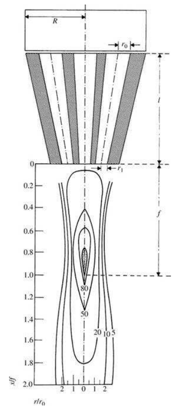

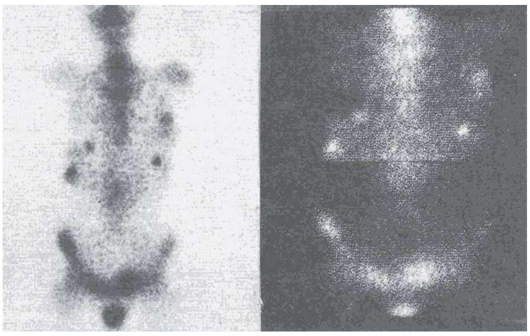

Figure 12.22 Images of a patient's skeleton obtained by a rectilinear scanner, in which a technetium-labeled phosphate compound reveals regions of abnormally high metabolism. The conventional analog image is on the left, the digitized version on the right.

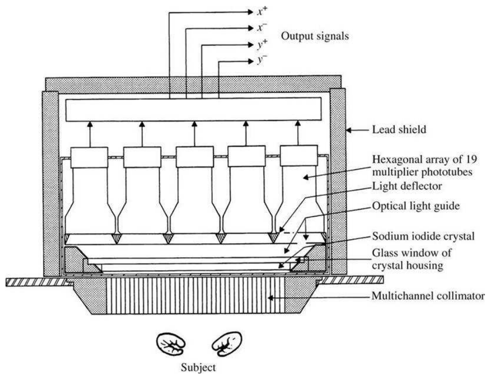

Figure 12.23 Cross-sectional view of a gamma camera (From G. J. Hine, ed., *Instrumentation in Nuclear Medicine.* New York: Academic, 1967.)

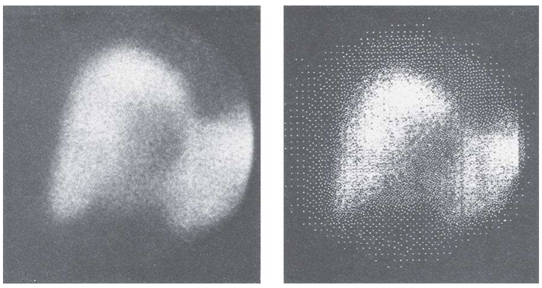

Figure 12.24 Gamma-camera images of an anterior view of the right lobe of a patient's liver. A colloid labeled with radioactive technetium was swept from the blood stream by normal liver tissue. Left: conventional analog image. Right: digitized version of the same data.

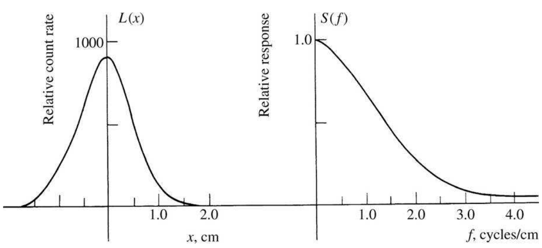

Figure 12.25 Line-spread response function obtained in a gamma camera under computer control, together with the corresponding modulation transfer function.

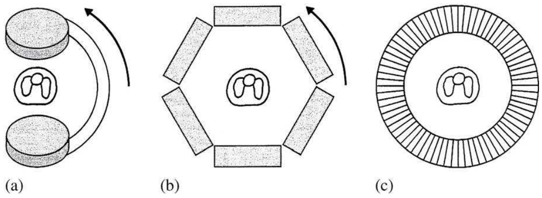

Figure 12.26 Evolution of the circular-ring PET camera (a) The paired and (b) the hexagonal ring cameras rotate around the patient, (c) The circular ring assembly does not rotate but may move slightly—just enough to fill in the gaps between the detectors. The solid-state detectors of the ring camera are integrated with the collimator and are similar in construction to detectors used in CT machines.

Table 12.2 Characteristics of Five Isotopes for PET

Isotope	Maximal Kinetic Energy	Half-life	Broadening
^{10}F	640 keV	110 min	1.1 mm
^{11}C	960 keV	20.4 min	1.9 mm
^{13}N	1.2 MeV	10.0 min	3.0 mm
^{60}Ga	1.9 MeV	62.3 min	5.9 mm
^{82}Rb	3.4 MeV	1.3 min	13.2 mm

Table 12.2

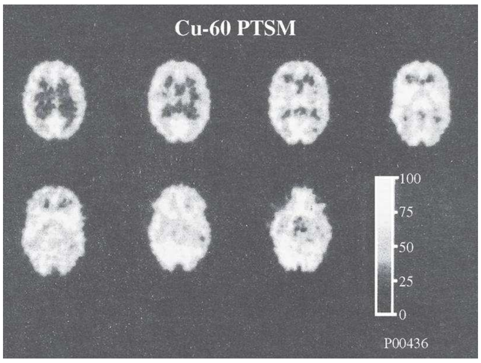

Figure 12.27 PET image The trapping of 60Cu-PTSM (a thiosemicarbazone) reflects regional blood flow, modulated by a nonunity extraction into the tissue. (Photo courtesy of Dr. R. J. Nickles, University of Wisconsin.)

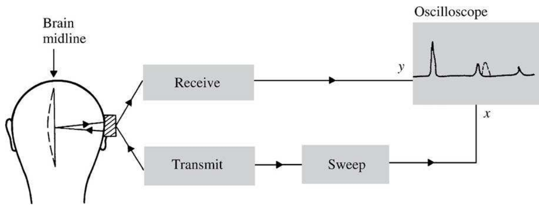

$$R = \left(\frac{Z_2 - Z_1}{Z_2 + Z_1}\right)^2$$

$$I = \frac{I_0 e^{-\alpha r}}{r^2}$$

Figure 12.28 A-mode scan of the brain midline

Table 12.3 Acoustic Properties of Some Tissues at 1.0 MHz

Tissue	*u*, m/s	*Z*, g/(cm²·s)	HVL, cm		*R* at Interface
Water	1496	1.49×10^5	4100	Air/water	0.999
Fat	1476	1.37×10^5	3.8	Water/fat	0.042
Muscle	1568	1.66×10^5	2.5	Water/muscle	0.054
Brain	1521	1.58×10^5	2.5	Water/brain	0.029
Bone	3360	6.20×10^5	0.23	Water/bone	0.614
Air	331	4.13	1.1	Tissue/air	0.999

Table 12.3

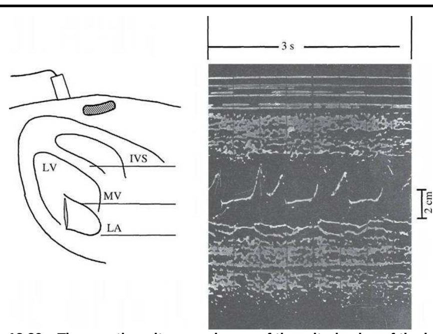

Figure 12.29 Time-motion ultrasound scan of the mitral valve of the heart The central trace follows the motions of the mitral valve (MV) over a 3 s period, encompassing three cardiac cycles. The other traces correspond to other relatively static structures, such as the interventricular septum (TVS) and the walls of the left atrium (LA).

Figure 12.30 (a) B-mode ultrasonic imaging shows the two-dimensional shape and reflectivity of objects by using multiple-scan paths, (b) This B-mode ultrasonic image, which corresponds to (a), shows the skin of the belly at the top right, the liver at the left center, the gall bladder at the right above center, and the kidney at the right below center. The bright areas within the kidney are the collecting ducts.

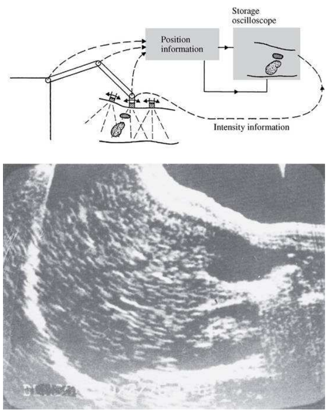

Figure 12.31 Different types of ultrasonic transducers range in frequency from 12 MHz for ophthalmic devices to 4 MHz for transducers equipped with a spinning head. (Photo courtesy of ATL.)

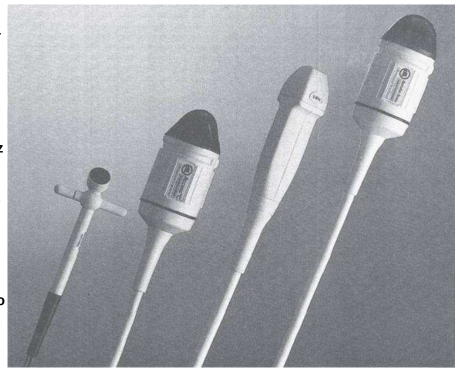

Figure 12.32 Ultrasound scan heads, (a) Rotating mechanical device, (b) Linear phased array which scans an area of the same width as the scan head, (c) Curved linear array can sweep a sector, (d) Phasing the excitation of the crystals can steer the beam so that a small transducer can sweep a large area.

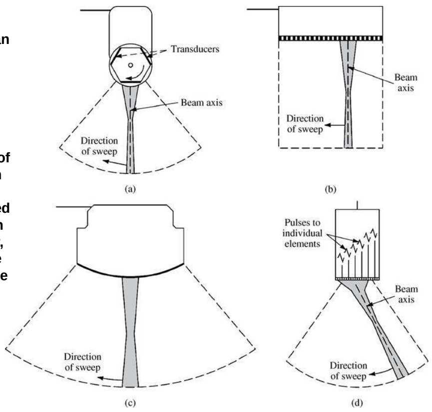

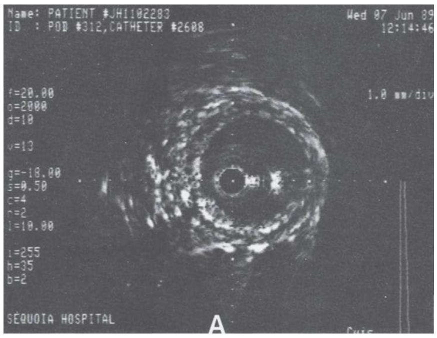

Figure 12.33 Intravascular ultrasonic image showing the characteristic three-layer appearance of a normal artery. Mild plaque and calcification can be observed at 7 o'clock. (Photo courtesy of Cardiovascular Imaging Systems, Inc.)

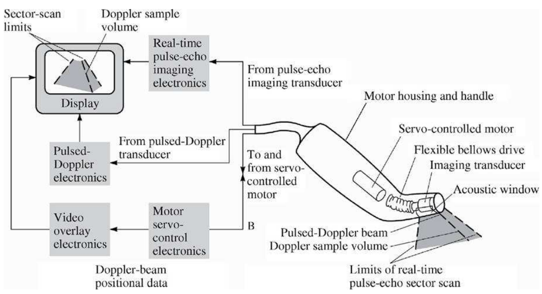

Figure 12.34 The duplex scanner contains a mechanical real-time sector scanner that generates a fan-shaped two-dimensional pulse-echo image. Signals from a selected range along a selected path are processed by pulsed Doppler electronics to yield blood velocity (from Wells, 1984).

Figure 12.35 (a) Duplex scanner B-mode image and Doppler spectral analysis record for a normal carotid artery, near the bifurcation. The Doppler signals were recorded from the sample volume defined by the Doppler cursor, the two parallel lines located inside the carotid artery, (b) Color flow image of the vessel in (a). Higher velocity components (lighter color, reproduced here in black and white) are seen where the vessel direction courses more directly toward the transducer.

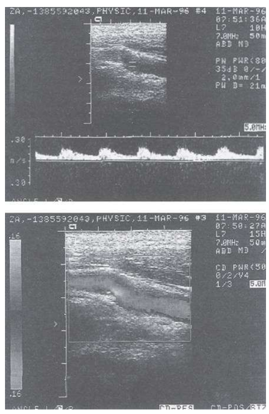

Figure 12.36
Angiogram of the author taken with iodine-based contrast agent. Image courtesy of Drs. Hinderaker and Farnham.